2014

An Algorithm to Estimate Unsteady and Quasi-Steady Pressure Fields from Velocity Field measurements

John O. Dabiri
California Institute of Technology

Sanjeeb Bose
Stanford University

Brad J. Gemmell
Woods Hole

Sean Colin
Roger Williams University, scolin@rwu.edu

John H. Costello
Providence College

Recommended Citation

Dabiri, J.O., S. Bose, Gemmell, S.P.Colin, J.H. Costello.2013. "An algorithm to estimate unsteady and quasi-steady pressure fields from velocity field measurements," *Journal of Experimental Biology* 217 (3): 331-336.

1 **An algorithm to estimate unsteady and quasi-steady pressure fields from velocity field**

2 **measurements**

3

4 John O. Dabiri[1*], Sanjeeb Bose[2], Brad J. Gemmell[3], Sean P. Colin[4], and John H. Costello[5]

5

6 [1]*Graduate Aeronautical Laboratories and Bioengineering, California Institute of Technology,*

7 *Pasadena, California 91125, USA*

8 [2]*Center for Turbulence Research, Stanford University, Stanford, California 94305, USA*

9 [3]*Whitman Center, Marine Biological Laboratory, Woods Hole, Massachusetts 02543, USA*

10 [4]*Marine Biology and Environmental Sciences, Roger Williams University, Bristol, Rhode Island*

11 *02809, USA*

12 [5]*Biology Department, Providence College, Providence, Rhode Island 02918, USA*

13

14 *Author for correspondence (email: jodabiri@caltech.edu)

15

16 Short title: Pressure estimation from velocity fields

17

18 Keywords: swimming, flying, wakes, feeding, particle image velocimetry

19

20 *Submitted to* Methods and Techniques *section of* Journal of Experimental Biology

21

22 **Summary**

23 We describe and characterize a method for estimating the pressure field corresponding to

24 velocity field measurements, such as those obtained by using particle image velocimetry. The

25 pressure gradient is estimated from a time series of velocity fields for unsteady calculations or

26 from a single velocity field for quasi-steady calculations. The corresponding pressure field is

27 determined based on median polling of several integration paths through the pressure gradient

28 field in order to reduce the effect of measurement errors that accumulate along individual

29 integration paths. Integration paths are restricted to the nodes of the measured velocity field,

30 thereby eliminating the need for measurement interpolation during this step and significantly

31 reducing the computational cost of the algorithm relative to previous approaches. The method is

32 validated by using numerically-simulated flow past a stationary, two-dimensional bluff body and

33 a computational model of a three-dimensional, self-propelled anguilliform swimmer to study the

34 effects of spatial and temporal resolution, domain size, signal-to-noise ratio, and out of plane

35 effects. Particle image velocimetry measurements of a freely-swimming jellyfish medusa and a

36 freely-swimming lamprey are analyzed using the method to demonstrate the efficacy of the

37 approach when applied to empirical data.

38

39

40 **Introduction**

41   A longstanding challenge for empirical observations of fluid flow is the inability to

42 directly access the instantaneous pressure field using techniques analogous to those established

43 to measure the velocity field. Recent approaches have made significant progress, especially in

44 the measurement of pressure associated with unsteady fluid-structure interactions (e.g. Hong and

45 Altman, 2008; Jardin et al. 2009a, 2009b; David et al., 2009; Rival et al. 2010a, 2010b; David et

46 al., 2012; Tronchin et al., 2012; van Oudheusden, 2013; Liu and Katz, 2013). However, prior

47 efforts have not achieved explicit pressure estimation for moving bodies with time-dependent

48 shape, such as those characteristic of animal locomotion and feeding. The pressure field of

49 swimming animals is complicated by the interaction between pressure associated with vortices in

50 the flow and the irrotational pressure field due to acceleration of the body, often referred to as the

51 acceleration reaction or added mass (Daniel, 1984).

52

2

53   Existing methods for empirical pressure estimation often require relatively complex

54   measurement techniques such as multi-camera or time-staggered, multi-exposure particle image

55   velocimetry (Jensen and Pedersen, 2004; Liu and Katz, 2006). In addition, significant

56   computational costs can be associated with the post-processing required to derive the pressure

57   field from measurements of the velocity or acceleration fields. These post-processing approaches

58   generally fall into one of two categories. In the first case, the pressure field is computed as a

59   solution to a Poisson equation, e.g. in an inviscid flow:

60

61    $$\nabla^2 p = -\rho\left(\nabla \cdot \frac{D\mathbf{u}}{Dt}\right),$$ (1)

62

63   where p is the pressure, $\mathbf{u}$ is the velocity vector, ρ is the fluid density, and D/Dt is the material

64   derivative, i.e., the time rate of change of an idealized infinitesimal fluid particle in the flow.

65   Solution of equation (1) poses challenges in practice because measurement errors accumulate

66   due to the required temporal and spatial derivatives of $\mathbf{u}$, the condition number (i.e. sensitivity)

67   of the Laplacian operator (Golub and Van Loan, 1996), and measurement uncertainty in the

68   boundary conditions, especially at fluid-solid interfaces (Gurka et al., 1999). For attached flows

69   at high Reynolds number, the Neumann boundary condition specifying the pressure gradient at

70   fluid-solid interfaces is given by the boundary layer approximation as $\partial p/\partial n \approx 0$, where n is the

71   direction of the local normal surface vector (Rosenhead, 1963). However, for separated flows at

72   moderate or low Reynolds numbers, such as those commonly found in animal locomotion, *a*

73   *priori* determination of the appropriate fluid-solid boundary conditions for solution of (1) can be

74   intractable.

75   A second category of approaches for pressure field estimation is those based on direct

76   integration of the pressure gradient term in the Navier-Stokes equation, e.g. for incompressible

77   flow:

78

79    $$\nabla p = -\rho\left(\frac{D\mathbf{u}}{Dt} - \nu\nabla^2\mathbf{u}\right)$$ (2)

80

81   where ν is the kinematic viscosity of the fluid. The pressure difference between two points in the

82   domain is determined by integration of equation (2) between the two points. For example, the

83   difference in pressure between two points $\mathbf{x}_1$ and $\mathbf{x}_2$ is given by

84

85    $$p_2 - p_1 = \int_{\mathbf{x}_1}^{\mathbf{x}_2} \nabla p \, d\mathbf{x} \qquad\qquad (3)$$

86

87   Because measurement errors accumulate along the path of integration from $\mathbf{x}_1$ to $\mathbf{x}_2$ in equation

88   (3), various techniques have been employed to make this approach less sensitive to measurement

89   uncertainty. A common strategy is to take advantage of the scalar property of the pressure field,

90   such that its local value is independent of integration path. Therefore, each independent

91   integration path that arrives at a point in the flow is in principle an independent estimate of the

92   pressure at that point, provided that measurement errors are uncorrelated. By polling a large

93   number of integration paths, an estimate of the local pressure can be achieved. For example, one

94   successful method (Liu and Katz, 2006) uses an iterative scheme that averages $2m(n+m) +$

95    $2n(2m+n)$ integration paths on an m x n grid in order to estimate the instantaneous pressure field.

96   The aforementioned iterative scheme, while effective in limiting the influence of

97   measurement errors, still incurs a relatively high computational cost. For example, for a 128 x

98   128 grid of velocity vectors that is commonly acquired using PIV, the method requires 1.6 x 10^5

99   integration paths per iteration of velocity field integration; and several iterations can be required

100   for convergence of the method (Liu and Katz, 2006). Furthermore, if each integration path is

101   taken as a straight line through the domain, then the method requires interpolation of the

102   estimated pressure gradient field in order to evaluate integration path points that do not coincide

103   with the original data grid. While these requirements are not necessarily prohibitive for two-

104   dimensional calculations, they are time-consuming and are indeed a showstopper for extension

105   of the method to three dimensions.

106   We present a simple yet demonstrably effective approach for pressure estimation that is

107   in the spirit of the second category of pressure estimation methods. The method is validated by

108   using two numerically-simulated flows: flow past a two-dimensional, stationary bluff body and

109   the flow created by a three-dimensional, self-propelled anguilliform swimmer. The first flow is

110   used to characterize a quasi-steady implementation of the algorithm, in which the pressure field

111   is estimated from a single velocity field measurement. The second flow demonstrates the ability

112   of the method to accurately estimate the pressure on unsteady, deformable bodies such as those

113   of relevance in animal locomotion. Both flows are used to characterize the method, including its

114   numerical convergence properties and sensitivity to domain size, signal-to-noise ratio, and out of

115   plane effects. Furthermore, we apply the method to PIV measurements of a freely-swimming

116   jellyfish medusa and a freely-swimming lamprey, showing that this tool can be applied to the

117   type of measurement data commonly acquired in research.

118

119   **Materials and Methods**

120   *Material acceleration estimation*

121   The instantaneous fluid particle acceleration $D\mathbf{u}/Dt$ required for calculation of the

122   pressure gradient in equation (2) is estimated by advecting idealized infinitesimal fluid particles

123   in the measured velocity fields. For quasi-steady estimation, the material acceleration is derived

124   from a single velocity field as

125

126    $$\frac{D\mathbf{u}}{Dt}(\mathbf{x}_i) \approx \frac{\mathbf{u}_{PIV}\left(\mathbf{x}_i^{\,a}\right) - \mathbf{u}_{PIV}(\mathbf{x}_i)}{\Delta t} \qquad\qquad (4)$$

127

128   where $i = 1, 2... \, m \times n$ (i.e. the dimensions of the velocity grid), $\mathbf{x}_i$ are the positions of fluid

129   particles coincident with the grid points in the PIV velocity field, and $\mathbf{x}_i^{\,a}$ are the positions of

130   those fluid particles after being advected by the instantaneous velocity field for a period Δt:

131

132    $$\mathbf{x}_i^{\,a} \approx \mathbf{x}_i + \mathbf{u}_{PIV}(\mathbf{x}_i)\Delta t \qquad\qquad (5)$$

133

134   In order for equations (4) and (5) to remain valid, Δt is limited to values much smaller

135   than the characteristic time scale of the flow, yet sufficiently large that there is a measurable

136   change in the fluid particle velocity.

137   For many flows, especially those involving accelerating or deforming bodies, the

138   aforementioned constraint on Δt cannot be satisfied. For these inherently unsteady fluid-structure

139   interactions, we derive the material acceleration from two sequential velocity fields as

140

141 $$\frac{D\mathbf{u}}{Dt}(\mathbf{x}_i, t_1) \approx \frac{\mathbf{u}_{PIV}(\mathbf{x}_i^{\ a}, t_2) - \mathbf{u}_{PIV}(\mathbf{x}_i, t_1)}{t_2 - t_1}$$ (6)

142 where $\mathbf{x}_i^{\ a} \approx \mathbf{x}_i + \left(\dfrac{\mathbf{u}_{PIV}(\mathbf{x}_i, t_1) + \mathbf{u}_{PIV}(\mathbf{x}_i, t_2)}{2} \right)(t_2 - t_1)$ (7)

143

144 Equation (7) is akin to a Crank-Nicolson (i.e. trapezoidal) scheme for the particle positions, in

145 contrast to the forward Euler scheme in equation (5). Hence, the convergence of the method with

146 time step is second order (Crank and Nicolson, 1947).

147 The primary source of measurement error in this type of unsteady estimate of the material

148 acceleration $D\mathbf{u}/Dt$ arises from temporal noise in the measured velocity components at each node

149 in the velocity field. We address this by applying a temporal filter to the time series of velocity

150 fields, which results in a smoothing spline approximation $\mathbf{u}^*$ to the velocity $\mathbf{u}$ at each node in the

151 velocity field. The spline approximations are defined such that they minimize, for each

152 component of $\mathbf{u}$, the parameter

153

154 $$S_{\mathbf{u}} = \phi \sum_{\tau=1}^{N} (\mathbf{u}_\tau - \mathbf{u}_\tau{}^*)^2 + (1 - \phi) \int_{t_{min}}^{t_{max}} \left(\frac{d^2 \mathbf{u}^*}{dt^2} \right)^2 dt$$ (8)

155

156 where $\tau = 1...N$ is the temporal sequence of velocity fields to be analyzed, $\mathbf{u}_\tau$ is a velocity vector

157 corresponding to velocity field τ in the sequence, $\mathbf{u}_\tau{}^*$ is the spline-approximated value of the

158 same velocity vector for the same velocity field in the sequence, t_{min} and t_{max} are the temporal

159 bounds on the sequence of velocity fields, and ϕ is a weight between the first and second terms

160 and has a value between 0 and 1. In effect, the parameter $S_{\mathbf{u}}$ quantifies both the deviation of the

161 spline approximation from the original data (i.e. the first term) and the total curvature magnitude

162 of the spline approximation (i.e. the second term). For $\phi = 0$, only the second term is minimized,

163 resulting in a least-squares fit with zero curvature, i.e. a linear fit to the data. For $\phi = 1$, only the

164 first term is minimized, giving a cubic spline fit that passes through each original data point. In

165 all that follows, we set $\phi = 0.05$, a value we have identified as enabling effective temporal noise

166 filtering without discarding true temporal trends in the measurement data.

167   Further characterization of the temporal filter is provided in Appendix 2. In particular, it

168   is shown that the use of the temporal filter increases the order of temporal convergence above

169   second order, as anticipated by theory (Atkinson, 1968).

170   It is worth noting that the distinction between the quasi-steady and unsteady approaches

171   can be made explicit by decomposing the material acceleration into its Eulerian components:

172

173     $$\frac{D\mathbf{u}}{Dt} \equiv \frac{\partial \mathbf{u}}{\partial t} + (\mathbf{u} \cdot \nabla)\mathbf{u} \tag{9}$$

174

175   The quasi-steady approximation in equations (4) and (5) implicitly neglects the first term on the

176   right-hand side of equation (9), whereas the unsteady calculation retains it.

177   The viscous term on the right-hand side of equation (2) is computed using centered finite

178   differences between adjacent nodes in the velocity field. The effect of the viscous term is

179   evaluated in the context of a numerical simulation described in the validation section.

180

181   *Pressure gradient integration*

182   Whereas previous methods that integrate the pressure gradient via many integration paths

183   assign to each grid point the arithmetic mean of the many integrations, in the present approach

184   the paths are polled by taking the median. The median is less sensitive to grossly erroneous

185   values that may arise on a few of the integration paths due to localized measurement errors or

186   due to localized errors created by the aforementioned material acceleration approximations in

187   equations (4) through (7). Hence, this approach enables a significant reduction in the total

188   number of integration paths per frame that are required to achieve accurate pressure estimates.

189   Fig. 1 illustrates the paths used presently. Eight families of integration paths are used, with each

190   family originating at the domain boundary and propagating toward each grid point from the left

191   (L), upper left (UL), top (T), upper right (UR), right (R), lower right (LR), bottom (B), and lower

192   left (LL), respectively.

193   Only 8 integration paths (one per family) per grid point are used, for a total of $8m$ x n

194   paths per velocity field. For the aforementioned example grid of 128 x 128 velocity vectors, 1.3

195   x 10^5 integration paths are required, a 20 percent reduction from existing optimal methods (Liu

196   and Katz, 2006). More importantly, the integration paths are constrained to include only grid

7

197   points coincident with the original velocity field. For example, the UL integration path is

198   comprised of alternating integration steps in the -y and +x directions, originating at the domain

199   boundary and terminating at each grid point. Hence, no interpolation is required in order to

200   integrate the pressure gradient field. Furthermore, portions of many of the paths are redundant,

201   facilitating fast calculation using simple matrix manipulations. A forward Euler spatial

202   integration scheme is used throughout, resulting in first-order spatial convergence of the method

203   (see Appendix 1).

204   An important limitation of the present algorithm that arises from the trade-off between

205   speed and accuracy is that it assumes the pressure is zero at the point on the outer domain

206   boundary where each integration path is initiated. This does not imply, however, that the final

207   pressure estimate is constrained to be zero at the boundaries. Integration paths that originate from

208   the other domain boundaries and terminate at a given boundary may estimate a non-zero value of

209   pressure at the termination point. If the median of all paths terminating at that point on the

210   domain boundary is non-zero, then the final pressure estimate at that point will also be non-zero.

211   Note that for all points in the domain, the final pressure estimate is relative to a zero reference

212   pressure, as that is the pressure at the origin of each integration path. The impact of these

213   assumptions on the robustness of the technique is quantified below, and it is shown to be modest

214   for the external flows tested. At the same time, the net result of this tradeoff in the algorithm

215   design is a more than order-of-magnitude reduction in computational time compared to previous

216   methods (see Appendix 2).

217   A common source of localized error that can affect pressure estimates is the presence of

218   solid objects in the flow. Typical PIV measurements are often unreliable in the region close to

219   solid objects, which compromises pressure integration paths that cross the fluid-solid interface,

220   especially in previous methods that average the erroneous data instead of discarding it via

221   median polling (or in Poisson solvers that rely on the pressure gradient at the fluid-solid interface

222   as a boundary condition). In the present algorithm, integration paths that cross a fluid-solid

223   interface in the flow can be nullified by assigning the nodes nearest to the interface an undefined

224   pressure gradient. Hence, when that value is integrated along any integration path, the pressure

225   value for that path also becomes undefined and therefore does not contribute to the median

226   calculation.

227

228   *Validation data sets*

229   To validate the accuracy of the quasi-steady pressure estimates achieved using this

230   algorithm, a numerical simulation of flow past a two-dimensional square cross-section cylinder

231   at a Reynolds number of 100 was used. This numerical data set enabled quantification of the

232   effects of spatial resolution, domain size, and signal-to-noise ratio, while providing a known

233   pressure field standard for comparison (see Appendix 1). The numerical simulation was

234   executed using a solver that computes on arbitrary polyhedra (Ham and Iaccarino, 2004). In the

235   present case, a regular Cartesian mesh was utilized and subsequently interpolated onto coarser

236   grids of varying sizes typical of PIV data. The viscous term in equation (2) was retained in all of

237   the calculations to demonstrate the robustness of the median polling approach to errors normally

238   associated with application of the Laplacian operator. For all calculations of equations (4) and

239   (5) in this validation, we set $\Delta t = 0.01h/U_{max}$, where h is the mean grid spacing and U_{max} is the

240   maximum flow speed in the measurement domain. The results described below were insensitive

241   to order of magnitude larger and smaller values of Δt. Where noted, nearest-neighbor Gaussian

242   smoothing was applied both to the pressure gradient before integration and to the resulting

243   pressure field.

244   The accuracy of the fully unsteady pressure estimates was validated by using a published

245   numerical simulation of a three-dimensional, self-propelled anguilliform swimmer (Kern and

246   Koumoutsakos, 2006). The Reynolds number based on swimmer length and speed was

247   approximately 2400. Time steps between sequential velocity fields from $0.02T$ to $0.08T$ (where T

248   is the swimming stroke duration) were studied to quantify the temporal convergence of the

249   method. The validation results described below are based on calculations of equations (6) and (7)

250   using velocity fields separated by $0.02T$.

251

252   *Empirical data sets*

253   The present method was also applied to particle image velocimetry measurements of a

254   freely-swimming *Aurelia aurita* (Linnaeus, 1758) jellyfish medusa and a freely-swimming

255   *Anguilla rostrata* (LeSueur, 1817) lamprey to demonstrate the performance of the algorithm with

256   empirical data inputs and, in the case of the jellyfish, without treatment of fluid-solid interfaces.

257   The swimming Reynolds numbers of the jellyfish and lamprey were approximately 1000 and

258   10,000, respectively, and the time between sequential velocity fields was 5 ms ($t/T \approx 0.013$) and

259   4 ms ($t/T \approx 0.015$), respectively. Details of the PIV implementation can be found in published

260   literature (Colin et al., 2012).

261

262   **Results and discussion**

263   *Quasi-steady pressure estimation*

264   Fig. 2 compares an instantaneous pressure field from the numerical simulation of flow

265   past a stationary bluff body with the pressure field estimated from the corresponding velocity

266   field using the quasi-steady form of the present algorithm. A vector field spatial resolution of

267     $D/16$ (where D is the side length of the bluff body) is used in the horizontal and vertical

268   directions to mimic typical PIV measurements. The salient features of the flow, especially the

269   high pressure on the upstream face of the bluff body and the low pressure in the shear layers and

270   near-wake vortices, are well captured by the algorithm (see Appendix 1 for discussion of

271   discrepancies in the far wake). Furthermore, the maximum and minimum pressures in the field

272   are in quantitative agreement (Fig. A1). To be sure, nearest-neighbor Gaussian smoothing creates

273   a spurious thin layer of undefined pressure at the fluid-solid interface and moves the pressure

274   peak on the upstream face of the body away from the interface. However, the correct near-body

275   pressure can be recovered by increasing the grid resolution so that the nearest-neighbor filter

276   artifact on the body surface is limited to a smaller region very close to the body. Additional

277   surface pressure calculations for the quasi-steady case (Appendix 1) are based on a velocity

278   vector spacing of $D/64$. Note that a similar increase in resolution using a PIV camera would

279   require a concomitant reduction in the measurement window size due to limits on camera pixel

280   resolution.

281   Additional characterization of the quasi-steady algorithm is detailed in Appendix 1,

282   including analysis of spatial convergence; the relative contribution of each integration path to the

283   median pressure field; robustness to measurement noise; and the effects of domain size, fluid

284   viscosity, and fluid-solid interfaces.

285

286   *Unsteady pressure estimation*

287   Fig. 3 compares an instantaneous pressure field from the numerical simulation of a self-

288   propelled anguilliform swimmer with the pressure field estimated from the corresponding

289   velocity field using the unsteady form of the present algorithm. A vector field spatial resolution

290   of *L*/42 (where *L* is the length of the swimmer) is used in the horizontal and vertical directions.

291   No smoothing is applied to this data set in order to contrast the results with those in the previous

292   section and to limit the spatial extent of the region of undefined pressure near the fluid-solid

293   interface. The algorithm is effective in capturing the high-low pressure couples formed on the

294   sides of the swimmer head and tail as they accelerate in the positive-*y* direction; the low-high

295   pressure couple formed at the mid-body as it accelerates in the negative-*y* direction; and the

296   pressure in the wake vortices.

297   The importance of the unsteady term in equation (9) is illustrated by comparison with the

298   pressure field estimated using the quasi-steady approximation, shown in Fig. 3C. Low pressure

299   in the wake vortices is captured, but the high-low pressure couples on the body surface due to the

300   body added mass are missing entirely, as is the high pressure in the wake due to vortex added

301   mass (Dabiri, 2006). The comparison is further quantified in Fig. 4, which plots the pressure on a

302   contour surrounding the swimmer and immediately adjacent to the region of undefined pressure.

303   At each of the four phases of the swimming cycle shown, good agreement is achieved between

304   the pressure computed in the numerical simulation and the pressure estimated from the velocity

305   field using the unsteady algorithm. By contrast, the pressure estimated by the quasi-steady

306   algorithm is erroneous everywhere except near the forming wake vortex at the tail.

307   Additional characterization of the unsteady algorithm is provided in Appendix 2,

308   including analysis of temporal convergence and out-of-plane effects for three-dimensional flows.

309   To demonstrate the efficacy of the present method for analyzing empirically measured

310   velocity fields, Fig. 5 shows measured velocity and vorticity fields for the freely-swimming

311   jellyfish and lamprey (panels A and C) along with the corresponding pressure fields estimated

312   using the unsteady algorithm (panels B and D). The full measurement domain is shown in both

313   cases; the velocity vector field is plotted at half of the full resolution. Only the left half of the

314   jellyfish body is visible in the measurement domain; its exumbrellar surface is indicated by a

315   black curve in panels A and B. The full lamprey body is visible in panels C and D.

316   In both cases, the pressure field derived from the velocity field measurements captures

317   key features near the body surface and in the wake. In particular, the jellyfish data set indicates

318   low pressure in the forming starting vortex and high pressure where the bell margin is

319   accelerating inward and pushing the adjacent fluid. The results are consistent with the measured

320   vorticity field (panel C), with the region of low pressure corresponding to the core of the starting

321 vortex. The presence of low and high pressure regions near the bell margin is also in agreement

322 with previous numerical simulations of a swimming jellyfish with similar body shape and

323 kinematics (Sahin et al., 2009).

324   The lamprey data set shares similarities with the three-dimensional numerical model

325 shown previously. The vorticity and pressure fields are less smooth and show finer structure in

326 the empirical measurements, which is attributable in part to the Reynolds number being

327 approximately four times higher than that of the numerical simulation.

328   The ease of implementation of this algorithm, both in terms of data acquisition and

329 velocity field post-processing, and its relatively low computation cost (see Appendix 2) gives it

330 the potential to find use in a broad range of problems of interest in biological fluid mechanics.

331 Because the temporal filter implemented in the unsteady algorithm does add considerable time to

332 the pressure calculation (cf. Fig. A10), in practice one should first evaluate the results of both the

333 quasi-steady and the fully unsteady implementations of the algorithm on a sample of the data of

334 interest to determine whether unsteady effects are important. If they are not, then the quasi-

335 steady calculation provides the most efficient tool for determination of the pressure field.

336   Although the present evaluation focused on two-dimensional velocity fields, it is

337 straightforward to extend the algorithm to three dimensions by the addition of a limited number

338 of new integration paths consistent with the geometry in Fig. 1. In that case, even greater

339 reductions in computation expense can be achieved relative to existing methods due to the

340 relatively small total number of required integration paths and the elimination of associated

341 velocity field interpolation during integration of the pressure gradients.

342   A free MATLAB implementation of this algorithm is available at

343 http://dabiri.caltech.edu/software.html.

344

345 **Appendix 1: Additional Characterization of Quasi-steady Algorithm**

346 *Effect of median polling*

347   To illustrate the contribution of each integration path to the final pressure estimate, Fig.

348 A1 plots the pressure on the body surface (at $0.1D$ away from the fluid-solid interface, to avoid

349 the spatial filter artifact) and on two additional concentric square contours in the domain (e.g. the

350 dashed contour in Fig. A2A), as computed using each of the 8 families of integration paths. The

351 results illustrate the benefit of median polling versus an average of the integration path results.

352 For example, only 5 of the integration path families intersect the upstream face of the bluff body

353 without passing through the body itself. The median of these curves is in good quantitative

354 agreement with the correct surface pressure (Fig. A1A). The pressure profiles for the two

355 concentric square contours in the domain (i.e. Figs. A1B and A1C) indicate that the contribution

356 of each family to the final pressure estimate is spatially non-uniform. This is illustrated

357 qualitatively in Fig. A1D, which is a contour plot that colors each point in the domain according

358 to the path family that corresponds to the median pressure at that point. Because there are 8 path

359 families, the median is always the average of the two intermediate values (where none of the

360 paths is undefined due to intersection with the solid body). To reveal the individual integration

361 path family contributions, a ninth pressure value equal to the mean of the 8 path families is

362 included in Fig. A1D, so that the median pressure is from either a single integration path family

363 or from the mean. The contour plot indicates that each integration path family contributes to the

364 final pressure field estimate, but the contributions are often spatially localized. The pressure

365 estimates for the R family of integration paths are noticeably less accurate than the other families

366 (e.g. Fig. A1A) and yet, as illustrated in Fig. A1D, these paths determine the pressure estimate in

367 the far wake. This leads to the observed poorer pressure estimate in that region of the flow (e.g.

368 Fig. 2B). The underlying source of this effect is discussed below in the section examining the

369 effect of boundary conditions.

370

371 *Effect of global measurement error*

372   Perhaps the most important test of the algorithm is its robustness to global measurement

373 errors, such as those associated with empirical measurements. Fig. A2 illustrates the streamwise

374 velocity contours for data sets with increasing levels of Gaussian white noise superimposed on

375 the *u* and *v* velocity components. The highest levels of noise, corresponding to the lowest signal-

376 to-noise ratios, are higher than typical PIV data but possibly representative of instantaneous two-

377 dimensional data collected in a highly-turbulent flow field, where out-of-plane motion can

378 reduce data quality. Comparison of the pressure profiles on a square contour centered on the

379 bluff body and with side length $3D$ so that it passes through the salient flow features (i.e. Fig.

380 A2A) indicates that, with the exception of the highest noise level tested, the quantitative pressure

381 estimates remain consistent with the noise-free result despite relatively high noise (Fig. A3A).

382   Error in the pressure estimate is not additive with the increasing noise level because

13

383   errors do not accumulate uniformly on the 8 paths that arrive at each point in the domain. Hence,

384   median polling remains an effective filter irrespective of the noise magnitude, up to the second-

385   highest noise level tested. At higher noise levels, contour plots of the pressure estimate begin to

386   exhibit spatial discontinuities reminiscent of the median contributions in Fig. A1D. Because the

387   pressure estimates from each integration path family begin to diverge in the presence of high

388   noise levels, median polling in this case leads to spatially discontinuous changes in pressure.

389   Result of this sort are an indication that measurement noise in the input velocity data has become

390   unacceptably large.

391

392   *Effect of boundary conditions*

393   As mentioned previously, a major assumption implicit in the present algorithm is that the

394   pressure on each integration path is zero at its originating point on the boundary, to avoid the

395   need for a computationally expensive iteration scheme to solve for the boundary pressure as part

396   of the field solution (Liu and Katz, 2006). Although this assumption can be reasonable for large

397   domains, it is prudent to investigate the dependence of the pressure estimate on the domain size.

398   Fig. A3B plots the pressure on a square contour centered on the bluff body (see Fig. A2A) for

399   domains ranging in size from $H/D = 2$ to 30, where H is the half-width of the domain. The results

400   indicate that the accuracy of the algorithm (and hence, the assumption regarding the boundary

401   pressure) is not significantly compromised until the domain shrinks to $H/D = 2$. This limitation is

402   important to keep in mind when designing experiments that will make use of the present

403   algorithm.

404   Notwithstanding the demonstrated efficacy of the aforementioned assumption regarding

405   the boundary pressure, examination of the individual pressure estimates on each family of

406   integration paths reveals that some individual estimates are severely compromised by this

407   assumption. Most notably, the R family of integration paths originate at the downstream

408   boundary of the domain, where vortices shed by the bluff body exit the measurement window

409   and create a non-zero pressure on that boundary. Hence this family of pressure estimates is

410   significantly less accurate than the others, as seen in Fig. A1A for example. The benefit of the

411   median polling approach is that this estimate is usually discarded in determining the final

412   pressure estimate. In contrast, previous methods would include pressure estimates affected by the

413   downstream boundary in the final averaged pressure estimate, and therefore require additional

414   computational effort to resolve the correct pressure on that boundary via iterative processes.

415   However, the present method does suffer in that the pressure in regions close to the

416   downstream boundary is based either on integration paths that originate at the downstream

417   boundary where the pressure is nonzero (i.e. R, UR, and LR families) or on long integration

418   paths from the other boundaries. The relatively large error accumulated on the long integration

419   paths can make them an even poorer estimate of the local pressure near the R boundary (cf. Fig.

420   A1D); hence the median pressure in this region is less accurate than in the rest of the domain.

421   This limitation is inherent in the present method and should be kept in mind when using the

422   technique for flows with large velocity gradients at any of the boundaries.

423

424   *Effect of fluid viscosity*

425   It is useful to examine the role of the viscous term in equation (2), as many previous

426   pressure estimation methods neglect this term. Fig. A4A plots the pressure estimates on the body

427   surface for each integration path family as in Fig. A1A, but for a pressure estimate that neglects

428   the viscous term in the Navier-Stokes equation. The effect is most noticeable in integration paths

429   orthogonal to the mean flow (i.e. T and B), especially near the upstream face of the bluff body.

430   This result can be understood by considering the contributions to the pressure gradient from the

431   streamwise and transverse material acceleration components, Du/Dt and Dv/Dt, relative to the

432   contributions from the Laplacian of the streamwise and transverse velocity components in the

433   viscous term. As the flow approaches the upstream face of the bluff body, the material

434   acceleration is dominated by streamwise fluid particle deceleration Du/Dt. However, the pressure

435   computed on integration paths that are orthogonal to the mean flow (i.e. T and B) is independent

436   of this term. Instead, on these paths the pressure depends to a significant degree on the local

437   velocity curvature (i.e. second spatial derivative) as the flow is turned around the bluff body.

438   This effect is captured in part by the Laplacian of the transverse velocity. Hence, its neglect leads

439   to an underestimate of the pressure on those integration paths. The net effect of the neglected

440   viscous term is minimal due to the median polling approach implemented presently, i.e., the T

441   and B paths do not represent the median pressure estimate on the upstream face of the bluff body

442   and are therefore not a factor in the final pressure estimate in that region of the flow.

443

444 *Effect of fluid-solid interfaces*

445   An aspect of the present algorithm that can be cumbersome is the treatment of the fluid-

446 solid interface to eliminate the effect of integration paths that pass through solid objects in the

447 flow. For example, for moving objects, this approach requires the identification of the fluid-solid

448 interface in each data frame. To illustrate the effect of the interface treatment in the algorithm,

449 Fig. A4B plots pressure estimates on the body surface, where the algorithm has been

450 implemented without treating the fluid-solid interface. The accuracy of the algorithm is

451 noticeably affected due to additional spurious pressure estimates on paths that cross the body.

452 However, it is noteworthy that the final pressure estimate is still qualitatively consistent with the

453 correct pressure field. It may therefore be acceptable to bypass the fluid-solid interface treatment

454 where only a quantitative approximation of the pressure field is sought. The results of the

455 analysis in Fig. 5B, which did not identify the boundary of the medusa as was done for the

456 numerical data, suggest that suitable pressure estimates can still be achieved where treatment of

457 the fluid-solid interfaces is not practical.

458

459 *Spatial convergence*

460   The spatial convergence of the quasi-steady algorithm was evaluated by computing the

461 pressure on a square contour immediately adjacent to the region of undefined pressure on the

462 bluff blody, and by integrating the pressure to compute the net force in the streamwise and lateral

463 directions. Fig. A5 plots the fractional error in these calculations (using the pressure from the

464 numerical simulation (CFD) as the true value, i.e. $\left|F_{CFD} - F_{estimate}\right|/F_{CFD}$) versus the grid

465 resolution. At relatively large grid spacing, the log-log curve has a slope of 1, indicating the

466 expected first-order spatial convergence of the method. As the grid spacing is further reduced,

467 the error decreases more slowly. This effect is due to a combination of inherent model error and

468 numerical round-off error. A convergence plot for calculations of the time-averaged streamwise

469 force is included. Its departure from first order convergence at small grid spacing confirms that

470 the quasi-steady approximation is not solely responsible for errors at small grid spacing. For grid

471 spacing less than $D/16$, the error falls below 5 percent for the instantaneous pressure and

472 approaches 10 percent for the time-averaged pressure.

473

Appendix 2: Additional Characterization of Unsteady Algorithm

Effect of temporal filter

Fig. A6 plots the time series of *v* component data at two selected points in the jellyfish PIV data set. Despite the relatively smooth spatial distribution of velocity, as illustrated in Fig. 5A and Fig. A7A, there is non-trivial scatter in the temporal data at both spatial locations. Flow accelerations computed by using finite differences of adjacent velocity fields would be subject to large errors because the local slope varies considerably between adjacent pairs of velocity fields. A temporal filter of the data is therefore essential in this case. Fig. A6 indicates the corresponding smoothing splines that were fit to the data and subsequently used to compute the material acceleration. The splines capture the true transient behavior of the flow while eliminating the high-frequency noise. Comparison of Fig. A7A and A7B illustrates that the spatial distribution of velocity is relatively unaffected by the temporal filter. It is prudent to note that if a flow exhibits real, high-frequency oscillations in the velocity, e.g. in turbulence, it will be essential that the PIV measurements are of sufficiently high temporal resolution such that the smoothing spline does not discard those temporal trends. In those cases, it is important that the frequency of PIV measurements satisfies the Nyquist sampling criterion with respect to the time scale of turbulence fluctuations, while concurrently avoiding sampling at frequencies high enough to incur numerical round-off errors in the calculation (Beckwith et al., 2007).

Effect of out-of-plane flow

Given that two-dimensional PIV data represents a projection of three-dimensional flow, it is useful to characterize the impact of that limitation on the accuracy of the present methods. As in prior work (Stamhuis and Videler, 1995), Fig. A8 characterizes the out-of-plane motion by computing the divergence of a two-dimensional velocity field extracted from the three-dimensional numerical simulation of the self-propelled swimmer and of the PIV data sets examined in Fig. 5. The divergence is made dimensionless by multiplying it by the time step between adjacent velocity fields, as this time scale is most relevant for calculation of the material acceleration. The plots effectively quantify the fractional change in the volume of an idealized infinitesimal fluid particle between adjacent velocity fields. Because the flows are incompressible, the fractional volume change would be identically zero if the flows were two-

17

504 dimensional. Deviation from zero values can therefore be attributed to velocity gradients

505 perpendicular to the plane of the velocity field, i.e., out-of-plane flow.

506 The results in Fig. A8 indicate that the three-dimensional numerical simulation exhibits

507 greater out-of-plane flow than the PIV measurements. Given the demonstrated accuracy of the

508 algorithm in the case of the three-dimensional numerical data, we can conclude that the

509 algorithm is robust to out-of-plane effects at the magnitudes found in typical PIV measurements.

510 To be sure, the divergence metric does not capture out-of-plane flow where there is no flow

511 gradient in the perpendicular direction. However, in such cases, the PIV would itself be difficult

512 to acquire, as the seed particles would not remain in the plane of the laser sheet sufficiently long

513 to enable temporal cross-correlation of their positions.

514

515 *Temporal convergence*

516 The temporal convergence of the unsteady algorithm was evaluated by plotting the

517 fractional error in the pressure at the head of the self-propelled swimmer at an instant of high

518 acceleration (using the pressure from the numerical simulation (CFD) as the true value, i.e.

519 $\left| p_{CFD} - p_{estimate} \right| / p_{CFD}$) versus the time step between velocity fields (Fig. A9). Although the

520 available data was limited to time steps from $0.02T$ to $0.08T$, the results are consistent with

521 temporal convergence that is higher than second order, except as the smallest step size is

522 approached, where further reduction in error is limited by inherent model error and numerical

523 round-off error. At a temporal spacing of $0.02T$, the error in the pressure at the head is

524 approximately 8 percent.

525 When the unsteady algorithm is applied to a sequence of velocity fields that are spaced

526 too closely in time, leading to increased numerical error, the results appear similar to those

527 described in the context of global measurement error (Appendix 1) in which the pressure

528 contours exhibit spatial discontinuity reminiscent of Fig. A1D.

529

530 *Computational cost*

531 Fig. A10 plots the time required for a single 3-GHz processor to apply the temporal filter

532 and to compute the pressure field for velocity fields from 32x32 to 256x256 nodes, which is a

533 practical upper limit for typical PIV measurements due to camera pixel resolution. The time

534 required for the temporal filter scales linearly with the number of nodes in the velocity field. The

18

cost is independent of the number of velocity fields in the sequence of up to the tested several

hundred frames of data. The computational cost of the subsequent pressure calculation scales

sublinearly in the range tested, and it is significantly lower than the cost of the temporal filter in

absolute terms. For example, for a 128x128 velocity field, each pressure field is computed in

approximately 3 seconds, as compared to 46 seconds using an existing iterative algorithm (Liu

and Katz, 2006).

Acknowledgments

References

Atkinson, K. E. (1968). On the order of convergence of natural cubic spline interpolation. *SIAM J. Numer. Anal.* **5**, 89-101.

Beckwith, T. G., Marangoni, R. D. and Lienhard V, J. H. (2007). *Mechanical Measurements*. Pearson Prentice Hall (New Jersey).

Costello, J. H., Colin, S. P., Dabiri, J. O., Villanueva, A., Blottman, J. B., Gemmell, B. J., Priya, S. (2012). Biomimetic and live jellyfish reveal the mechanistic advantages of a flexible bell margin. *PLoS ONE* **7**, e48909.

Crank, J. and Nicolson, P. (1947). A practical method for numerical evaluation of solutions of partial differential equations of the heat conduction type. *Proc. Camb. Phil. Soc.* **43**, 50-67.

Dabiri, J. O. (2006). Note on the induced Lagrangian drift and added-mass of a vortex. *J. Fluid Mech.* **547**, 105-113.

Daniel, T. L. (1984). Unsteady aspects of aquatic locomotion. *Am. Zool.* **24**, 121-134.

David, L., Jardin, T., Braud, P. and Farcy, A. (2012). Time-resolved scanning tomography PIV measurements around a flapping wing. *Exp. Fluids* **52**, 857-864.

566 **David, L., Jardin, T. and Farcy, A.** (2009). On the non-intrusive evaluation of fluid forces
567   with the momentum equation approach. *Meas.Sci. Technol.* **20**, 095401.

568 **Golub, G. H. and Van Loan, C. F.** (1996). *Matrix Computations*. The Johns Hopkins
569   University Press (Maryland).

570 **Gurka R., Liberzon, A., Hefetz, D., Rubinstein, D. and Shavit, U.** (1999). Computation of
571   pressure distribution using PIV velocity data. *International workshop on particle image*
572   *velocimetry*, 3rd ed., 671-676.

573 **Ham, F. and Iaccarino, G.** (2004). Energy conservation in collocated discretization schemes on
574   unstructured meshes. *Center for Turbulence Research Annual Research Briefs*, 3-14.

575 **Hong, Y. S. and Altman, A.** (2008). Lift from spanwise flow in simple flapping wings. *J. Aircr.*
576   **45**, 1206-1216.

577 **Jardin, T., Chatellier, L., Farcy, A. and David, L.** (2009). Correlation between vortex
578   structures and unsteady loads for flapping motion in hover. *Exp. Fluids* **47**, 655-664.

579 **Jardin, T., David, L. and Farcy, A.** (2009). Characterization of vortical structures and loads
580   based on time-resolved PIV for asymmetric hovering flapping flight. *Exp. Fluids* **46**, 847-
581   857.

582 **Jensen, A. and Pedersen, G. K.** (2004). Optimization of acceleration measurements using PIV.
583   *Meas. Sci. Technol.* **15**, 2275-2283.

584 **Kern, S. and Koumoutsakos, P.** (2006). Simulations of optimized anguilliform swimming. *J.*
585   *Exp. Biol.* **209**, 4841-4857.

586 **Liu, X. and Katz, J.** (2006). Instantaneous pressure and material acceleration measurements
587   using a four-exposure PIV system. *Exp. Fluids* **41**, 227-240.

588 **Liu, X. and Katz, J.** (2013). Vortex-corner interactions in a cavity shear layer elucidated by
589   time-resolved measurements of the pressure field. *J. Fluid Mech.* **728**, 417-457.

590 **Rival, D., Manejev, E. and Tropea, C.** (2010). Measurement of parallel blade-vortex
591   interaction at low Reynolds numbers. *Exp. Fluids* **49**, 89-99.

592 **Rival, D., Schönweitz, D. and Tropea, C.** (2010). Vortex interaction of tandem pitching and
593   plunging plates: a two-dimensional model of hovering dragonfly-like flight. *Bioinsp.*
594   *Biomim.* **6**, 016008.

595 **Rosenhead, L.** (1963). *Laminar Boundary Layers*. Dover (New York).

596 **Sahin, M., Mohseni, K. and Colin, S. P.** (2009). The numerical comparison of flow patterns
597   and propulsive performances for the hydromedusae *Sarsia tubulosa* and *Aequorea*
598   *victoria*. *J. Exp. Biol.* **212**, 2656-2667.

599 **Stamhuis, E. J. and Videler, J. J.** (1995). Quantitative flow analysis around aquatic animals
600   using laser sheet particle image velocimetry. *J. Exp. Biol.* **198**, 283-294.

601 **Tronchin, T., Farcy, A. and David, L.** (2012). Evaluation of pressure field and fluid forces for
602   3D flow around flapping wing *International workshop on the application of PIV for*
603   *aeroacoustics and* noise, 59-62.

604 **van Oudheusden, B. W.** (2013). PIV-based pressure measurement. *Meas. Sci. Technol.* **24**,
605   032001.

606
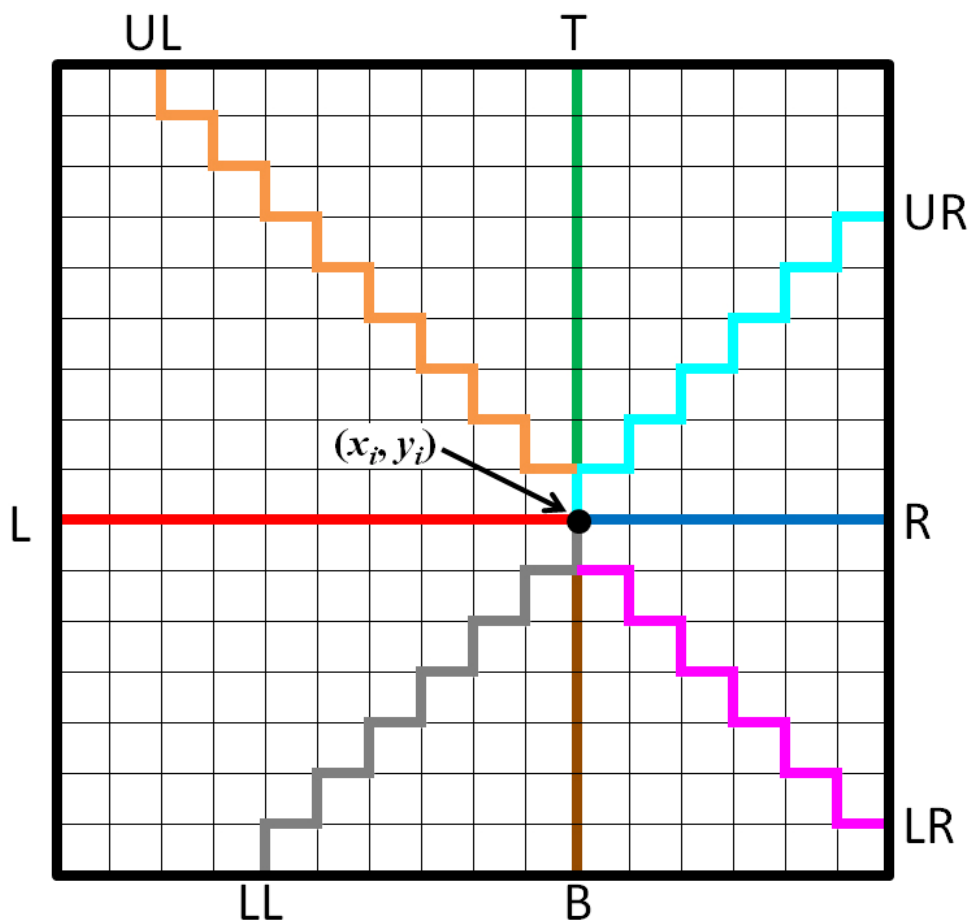
Figure 1. Geometry of integration paths for pressure field estimation. Eight paths originate from the domain boundary and propagate toward each point (x_i, y_i) in the domain from the left (L), upper left (UL), top (T), upper right (UR), right (R), lower right (LR), bottom (B), and lower left (LL). The points on each path coincide with the measurement grid.

611

612
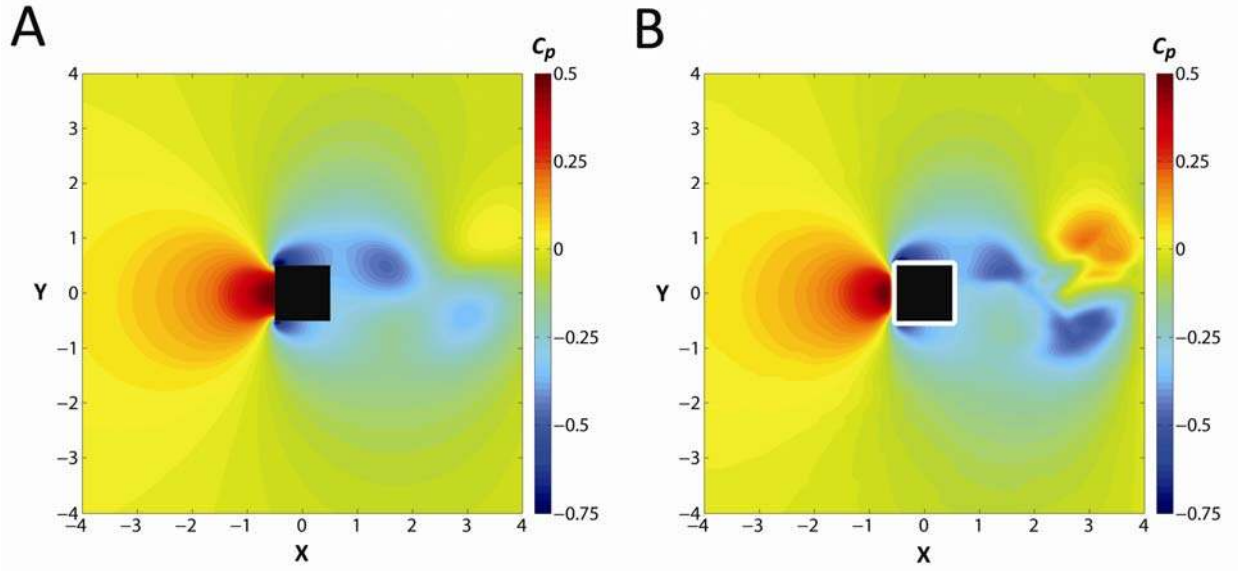
Figure 2. (A) Pressure field computed from numerical simulation of flow past two-dimensional

square cylinder at a Reynolds number Re $= UD/\nu = 100$. The pressure coefficient $c_p = p/(\rho U^2)$.

(B) Pressure field estimated using quasi-steady algorithm.

616
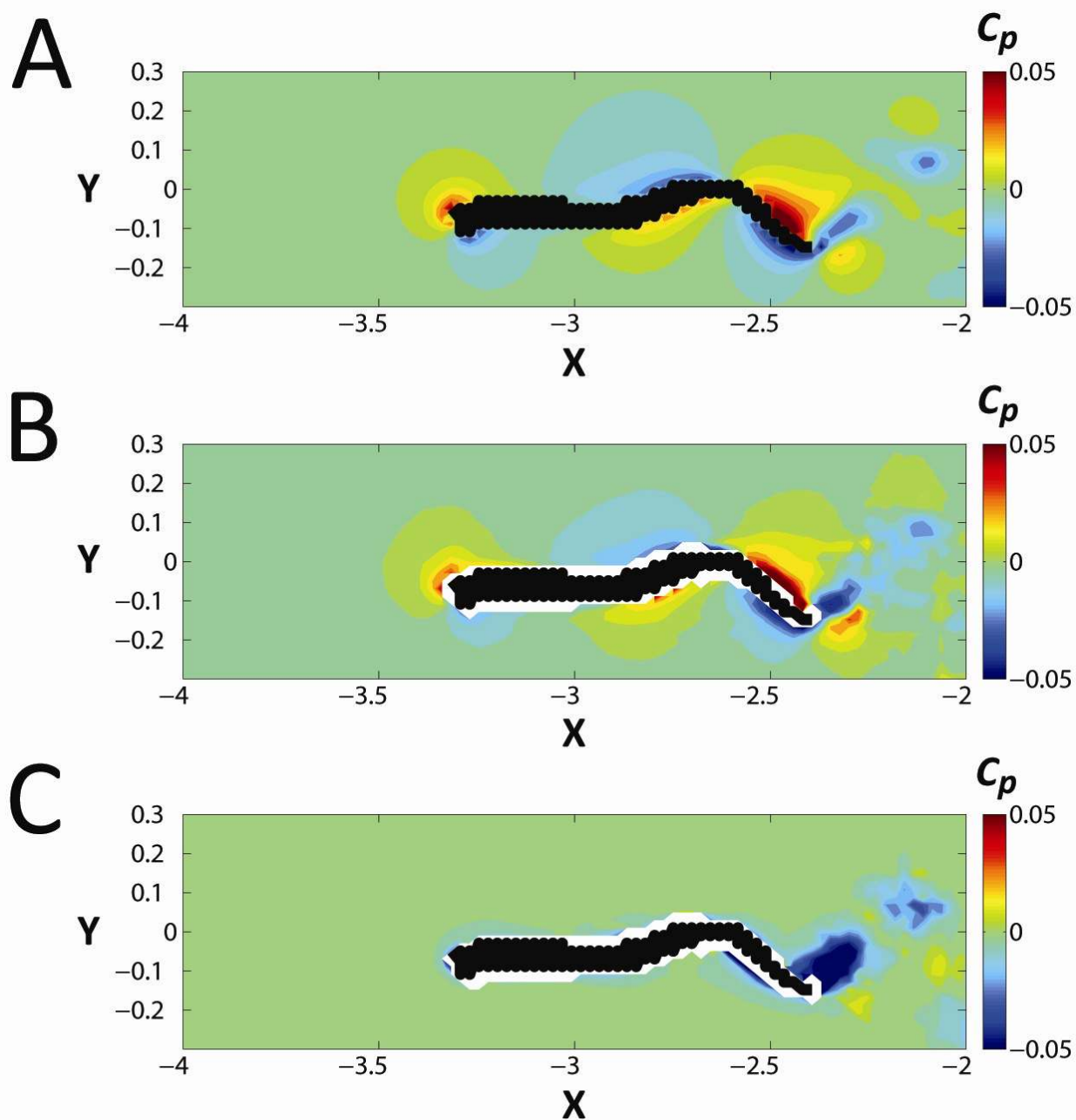
617

618 **Figure 3.** (A) Pressure field computed from numerical simulation of three-dimensional self-

619 propelled swimmer. The pressure coefficient $c_p = p/(\rho U^2)$. Velocity nodes completely inside

620 swimmer body are indicated in black (body surface is smooth in numerical simulation). Spatial

621 coordinates are normalized by swimmer length. (B) Pressure field estimated using unsteady

622 algorithm. (C) Pressure field estimated using quasi-steady algorithm.

623

624
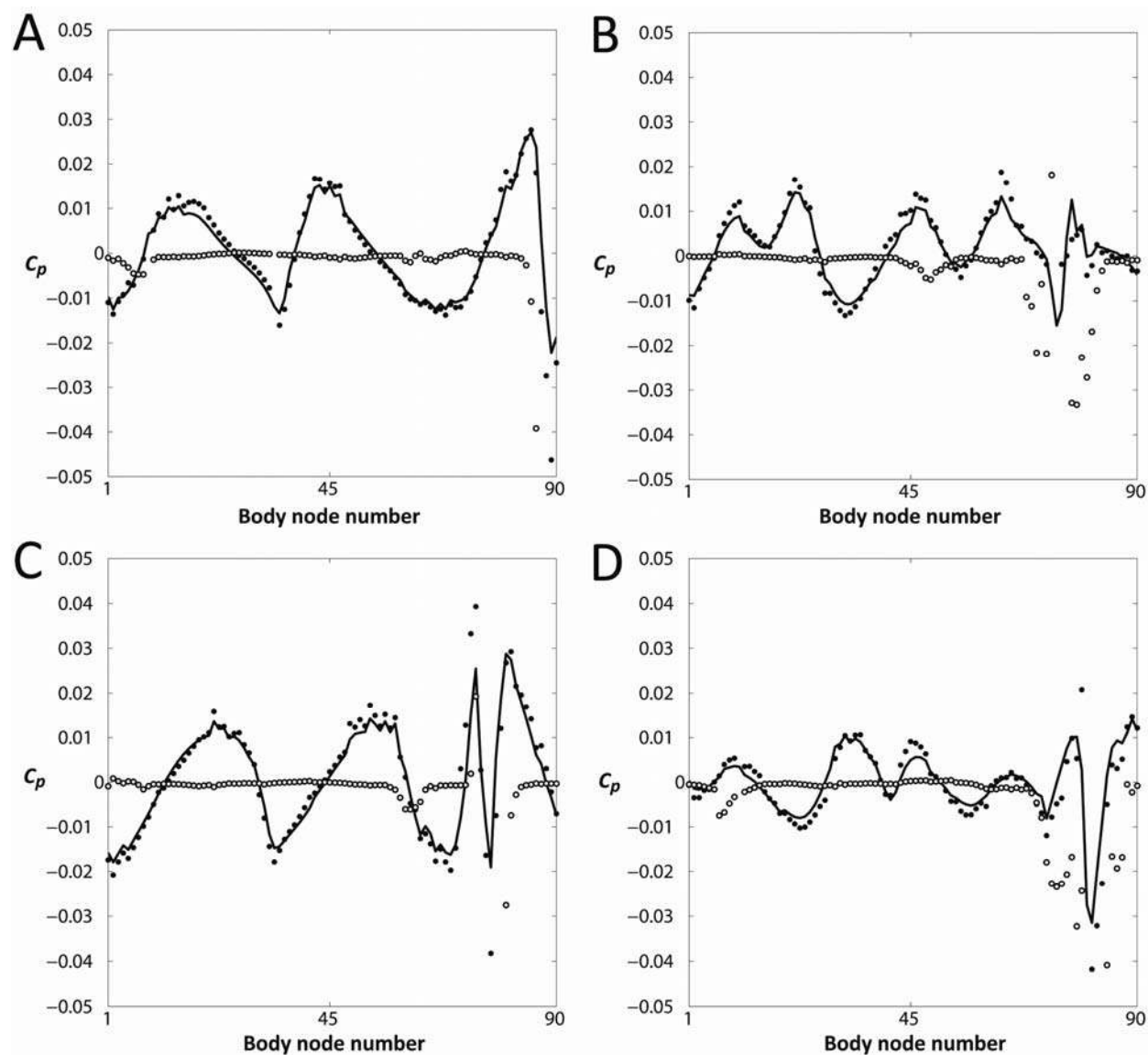
Figure 4. Pressure on contour surrounding the self-propelled swimmer and immediately adjacent

to the region of undefined pressure, at four instants during the swimming cycle duration T. Head

is at body node number 45; tail is at body nodes 1 and 90. Solid curve, pressure computed from

numerical simulation. Closed circles, pressure estimated from unsteady algorithm. Open circles,

pressure estimated from quasi-steady algorithm. (A) $t/T = 1/4$. (B) $t/T = 1/2$. (C) $t/T = 3/4$. (D)

$t/T = 1$.

631
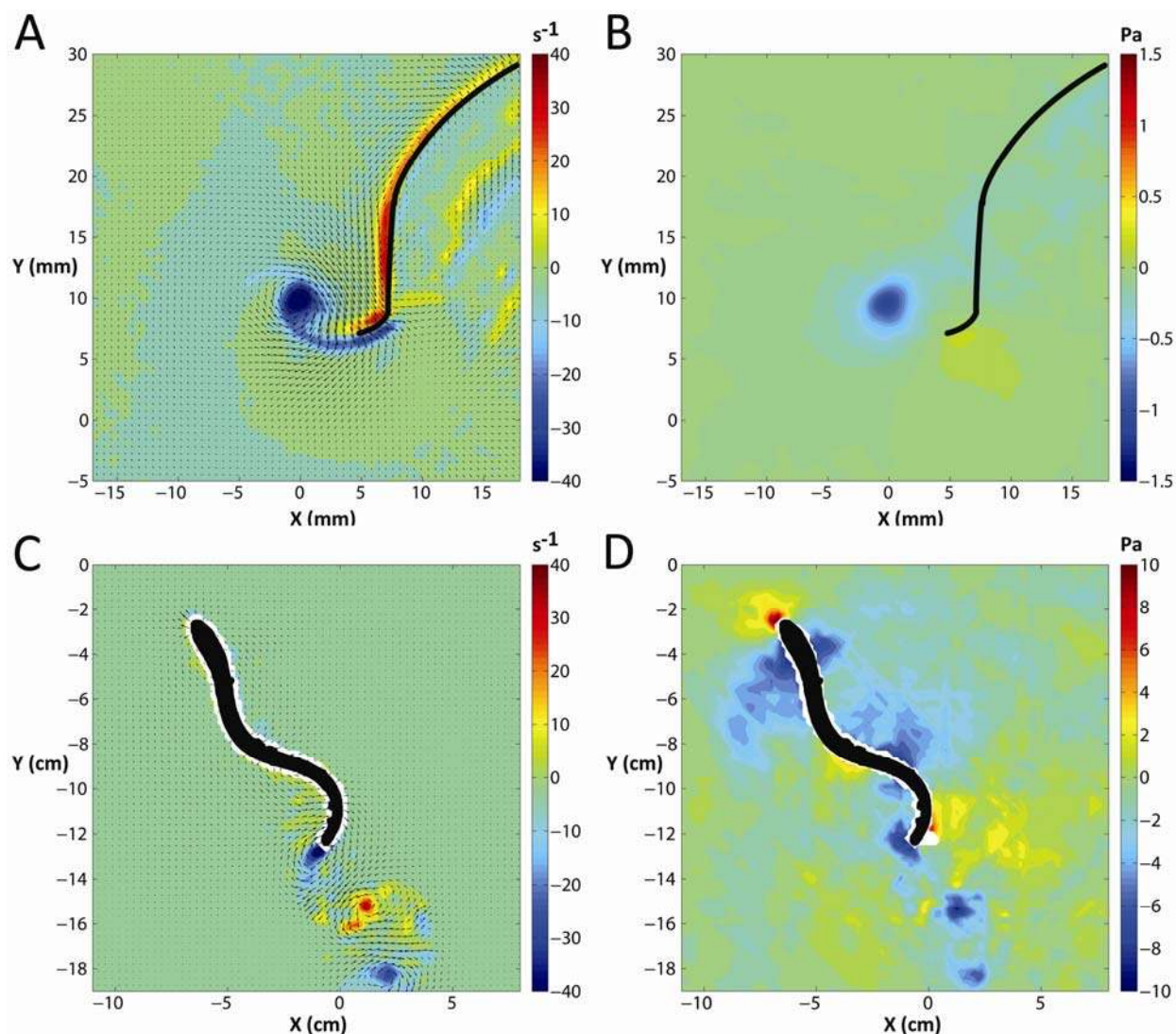
Figure 5. (A) Particle image velocimetry (PIV) measurement of a freely-swimming jellyfish

medusa. Velocity field is plotted on vorticity contours. Maximum velocity vector is

approximately 3 cm s^{-1}. Velocity field is plotted at half of full resolution. Left half of

exumbrellar surface is indicated by black curve. (B) Pressure field estimated using unsteady

algorithm. (C) Particle image velocimetry (PIV) measurement of a freely-swimming lamprey.

Velocity field is plotted on vorticity contours. Maximum velocity vector is approximately 11 cm

s^{-1}. Velocity field is plotted at half of full resolution. Animal body is approximately indicated in

black. (D) Pressure field estimated using unsteady algorithm.

640
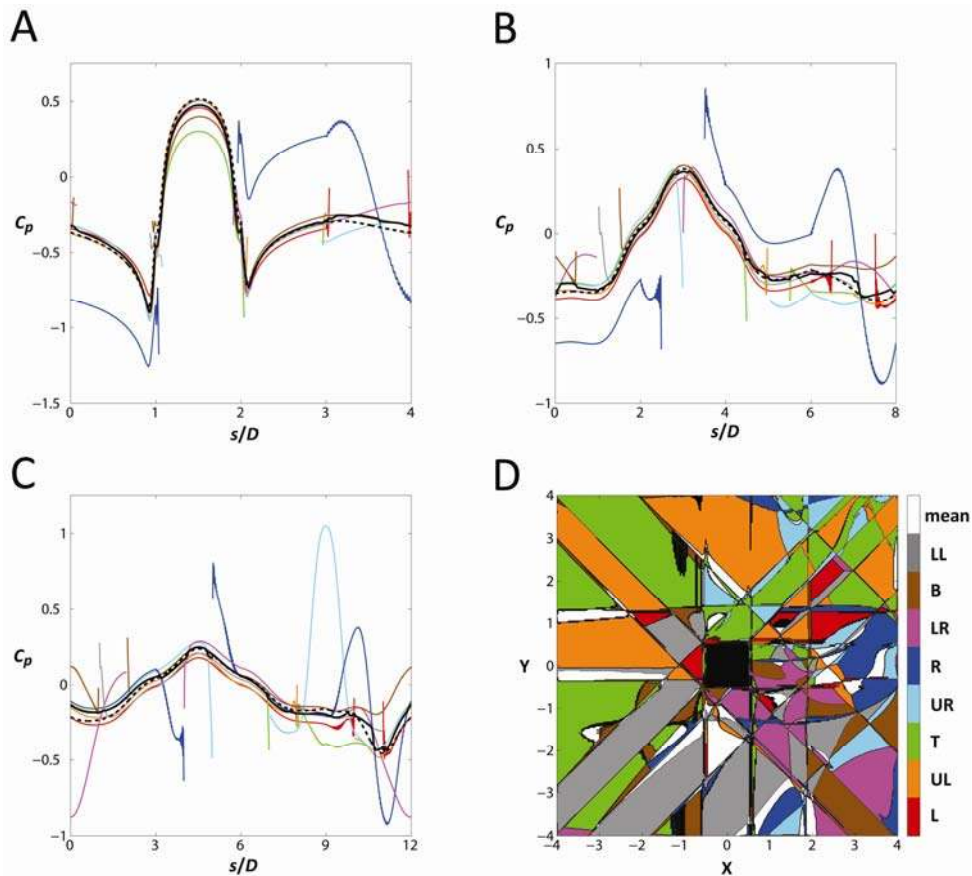
Figure A1. (A) Pressure on surface of bluff body estimated using quasi-steady algorithm. Measurement contour is offset by $0.1D$ from the fluid-solid interface. The pressure coefficient c_p = $p/(\rho U^2)$. s is the local surface coordinate and increases in the counter-clockwise direction from the upper right corner of the bluff body. Dashed black line, pressure from numerical simulation; solid black line, pressure estimated using quasi-steady algorithm; solid colored lines, pressure estimates based on each family of integration paths. Colors correspond to paths in Fig. 1 and to the legend in panel D. (B, C) Pressure on square contours centered on the bluff body and with side length $2D$ and $3D$, respectively (e.g. Fig. A2A). s is the local surface coordinate and increases in the counter-clockwise direction from the upper right corner of each square contour. The difference in abscissa in panels A-C reflects the different contour perimeters. (D) Contour plot that colors each point in the domain according to the path family that corresponds to the median pressure at that point. To reveal the individual integration path family contributions, a ninth pressure value equal to the mean of the 8 path families is included, so that the median pressure is from either a single integration path family or from the mean.
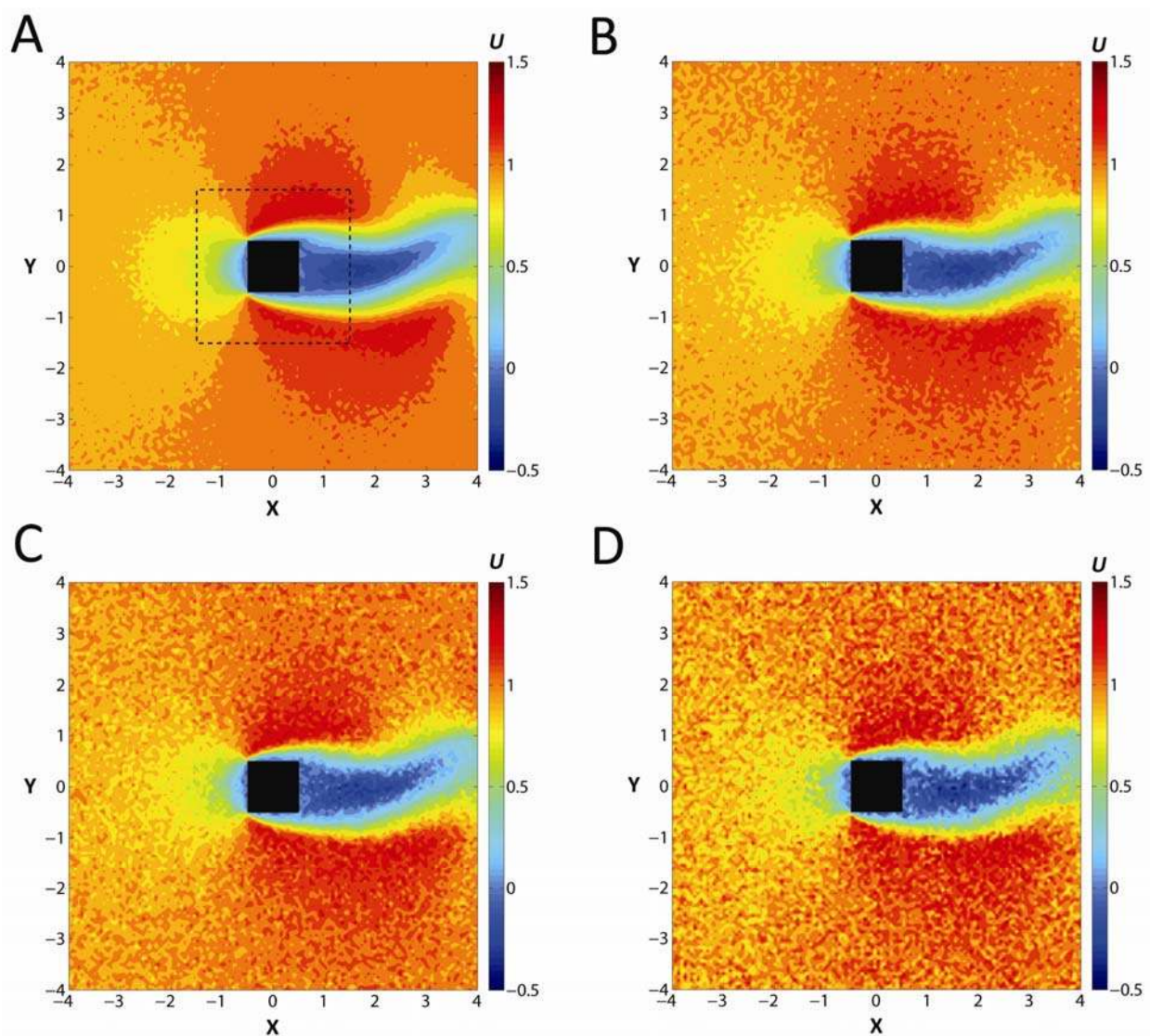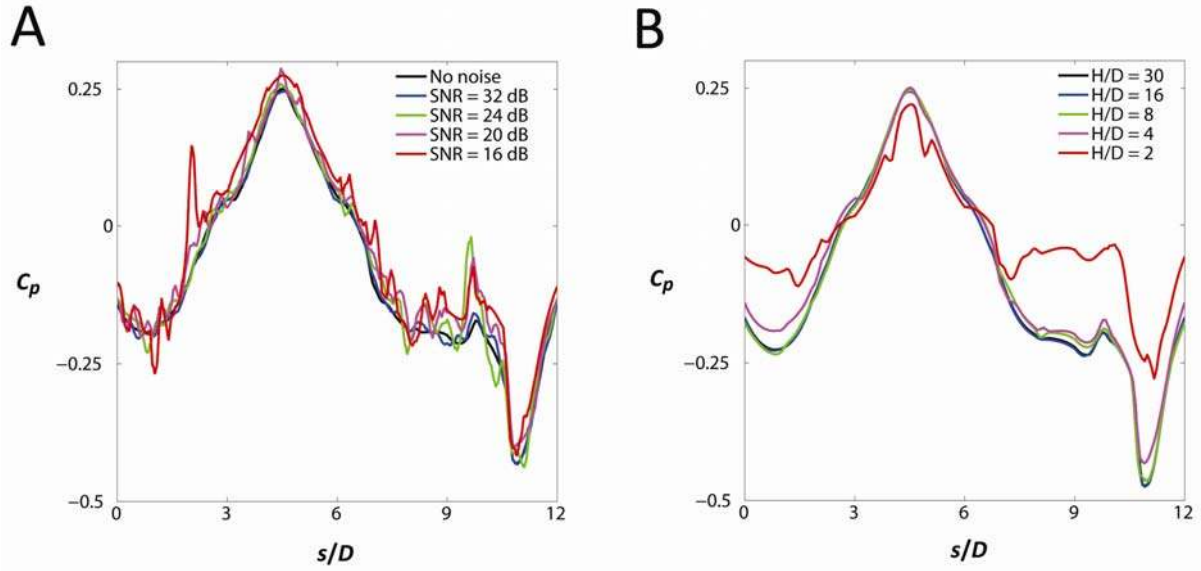
Figure A2. Streamwise velocity contours for flow field with Gaussian white noise added to reduce the signal-to-noise ratio (SNR). (A) SNR = 32 dB. (B) SNR = 24 dB. (C) SNR = 20 dB. (D) SNR = 16 dB. Dashed square in panel A indicates contour on which quasi-steady pressure estimates are compared in Fig. A3A.

662

663 **Figure A3.** (A) Quasi-steady pressure estimate on contour shown in Fig. A2A for varying signal-

664 to-noise ratio. *s* is the local surface coordinate and increases in the counter-clockwise direction

665 from the upper right corner of the square contour. (B) Quasi-steady pressure estimate on contour

666 shown in Fig. A2A for varying measurement domain size. *H* is the half-width of the

667 measurement domain.

668
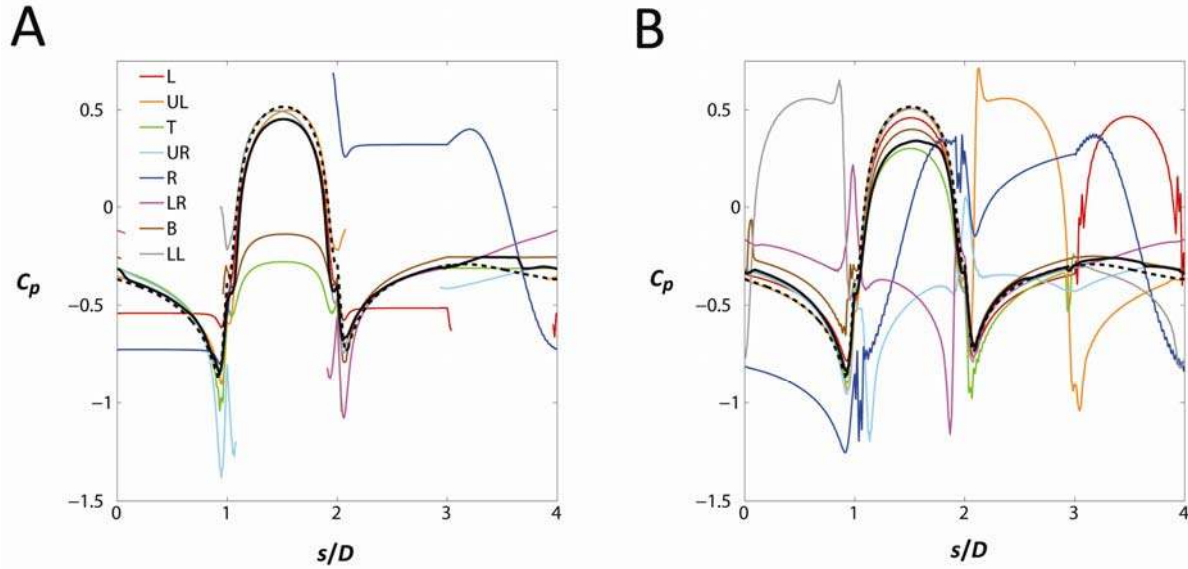
669

670   **Figure A4.** (A) Pressure on surface of bluff body estimated using quasi-steady algorithm without

671   viscous term. Measurement contour is offset by $0.1D$ from the fluid-solid interface. s is the local

672   surface coordinate and increases in the counter-clockwise direction from the upper right corner

673   of the bluff body. Dashed black line, pressure from numerical simulation; solid black line,

674   pressure estimated using quasi-steady algorithm; solid colored lines, pressure estimates based on

675   each family of integration paths. (B) Pressure on surface of bluff body estimated using quasi-

676   steady algorithm without treatment of fluid-solid interfaces to remove integration paths that pass

677   through the solid body.

678
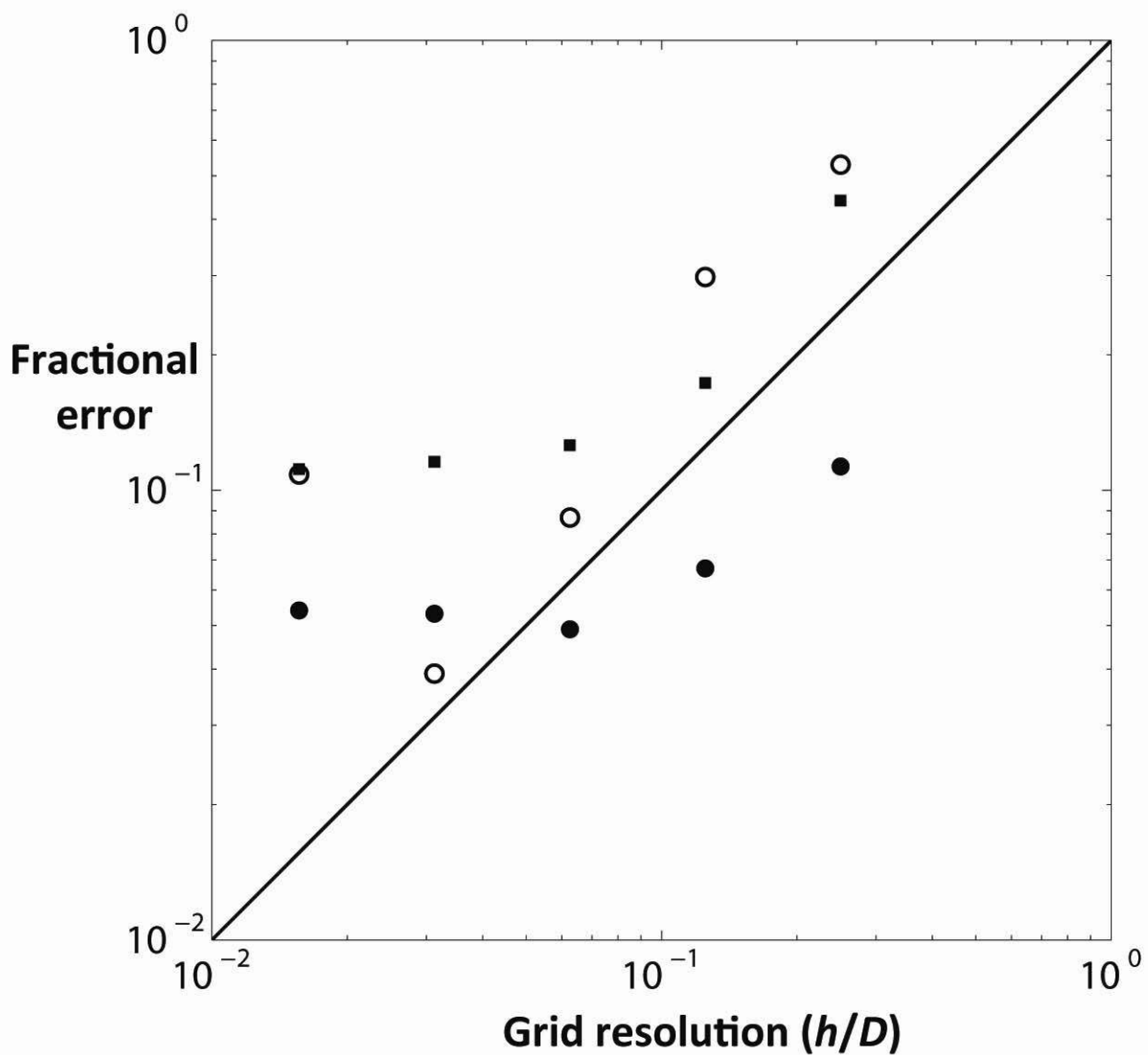
Figure A5. Spatial convergence of the algorithm. Log-log plot of the fractional error in instantaneous streamwise (closed circles), instantaneous lateral (open circles), and time-averaged streamwise (closed squares) force coefficients versus grid resolution for numerical simulation of two-dimensional flow past the bluff body. Solid line indicates a slope of 1 corresponding to first-order convergence. Deviation from first-order convergence at small grid resolution is due to a combination of model error and numerical round-off error.
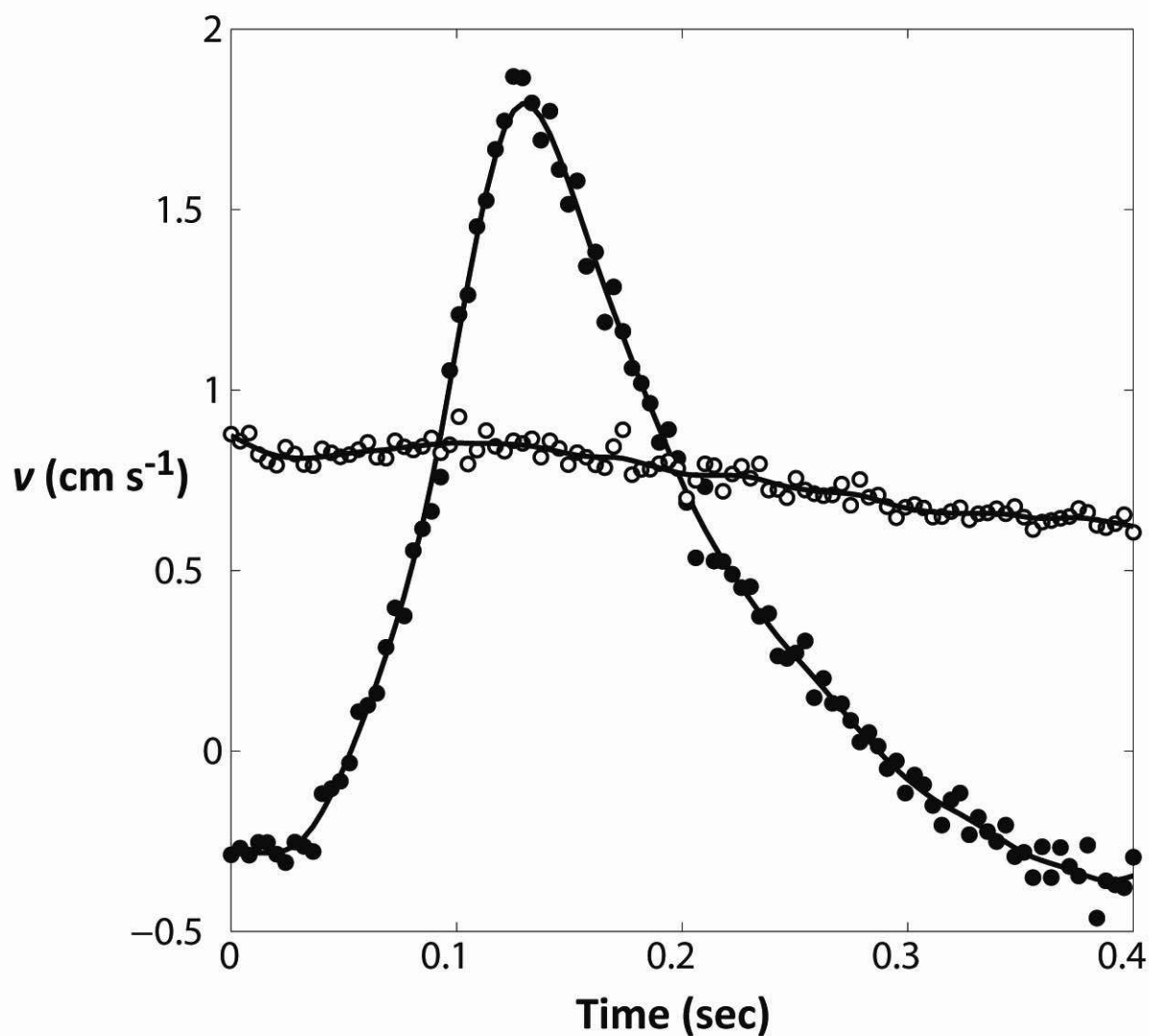
686

687 **Figure A6.** Time series of *v* component data at two selected points in the jellyfish PIV data set.

688 Symbols indicate original PIV data at corresponding locations identified in Fig. A7. Solid curves

689 indicate respective smoothing splines.

690
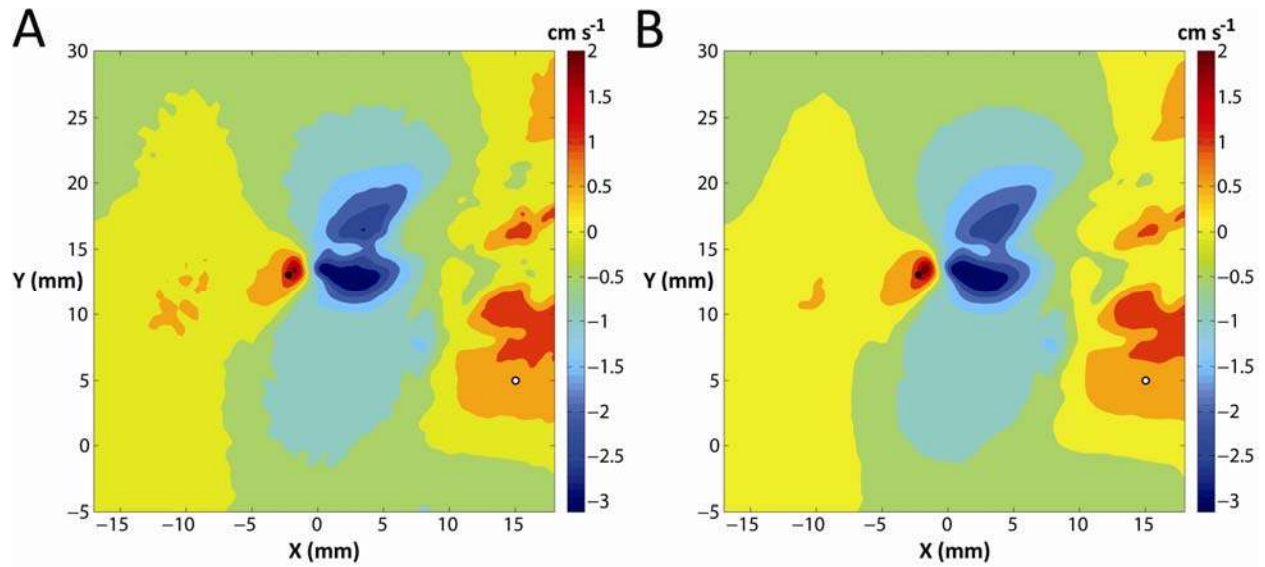
691

692 **Figure A7.** (A) Contour plot of *v* component of original velocity measurement during middle of

693 jellyfish bell contraction. (B) Contour plot of *v* component temporal spline-filtered velocity

694 measurement during middle of jellyfish bell contraction. Location of animal is similar to that

695 indicated in Fig. 5A, although earlier in the bell contraction phase. Closed circle near bell margin

696 and open circle in wake indicate locations of temporal profiles in Fig. A6.

697

698
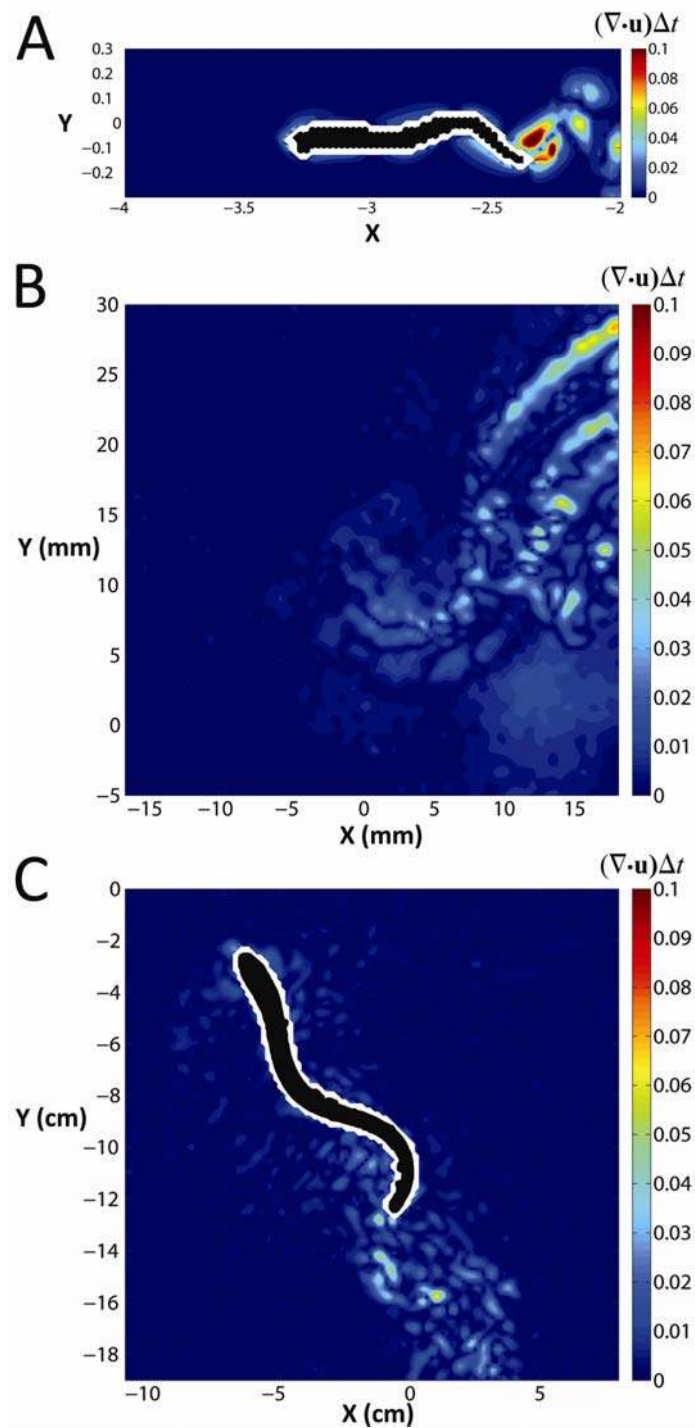
Figure A8. Contour plots of normalized two-dimensional divergence for (A) three-dimensional
numerical simulation of self-propelled swimmer, (B) PIV measurement of freely-swimming
jellyfish (cf. Fig. 5A), (C) PIV measurement of freely-swimming lamprey (cf. Fig. 5C).
Dimensional divergence is normalized by multiplying by the time step between sequential
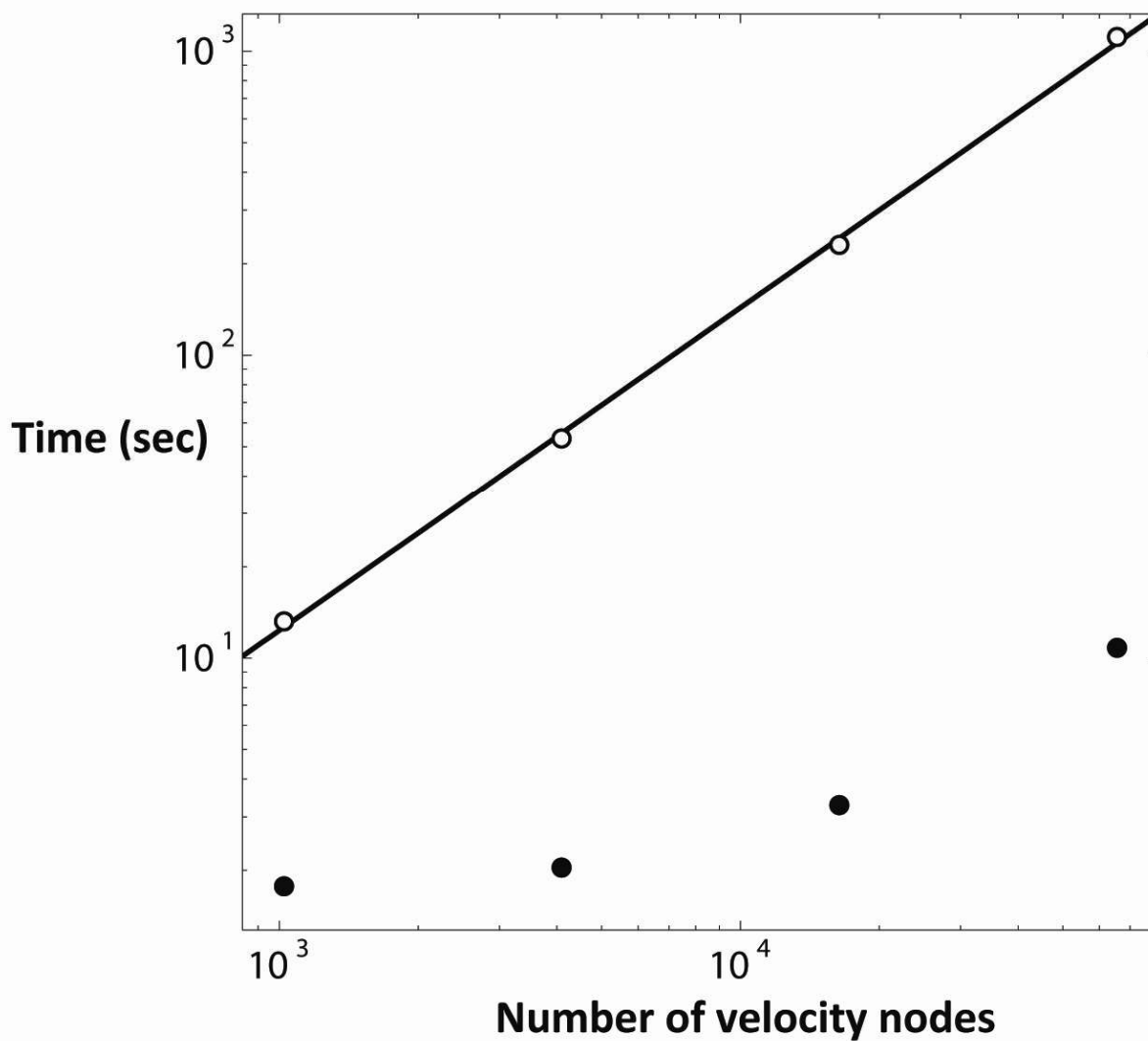velocity fields in each case.
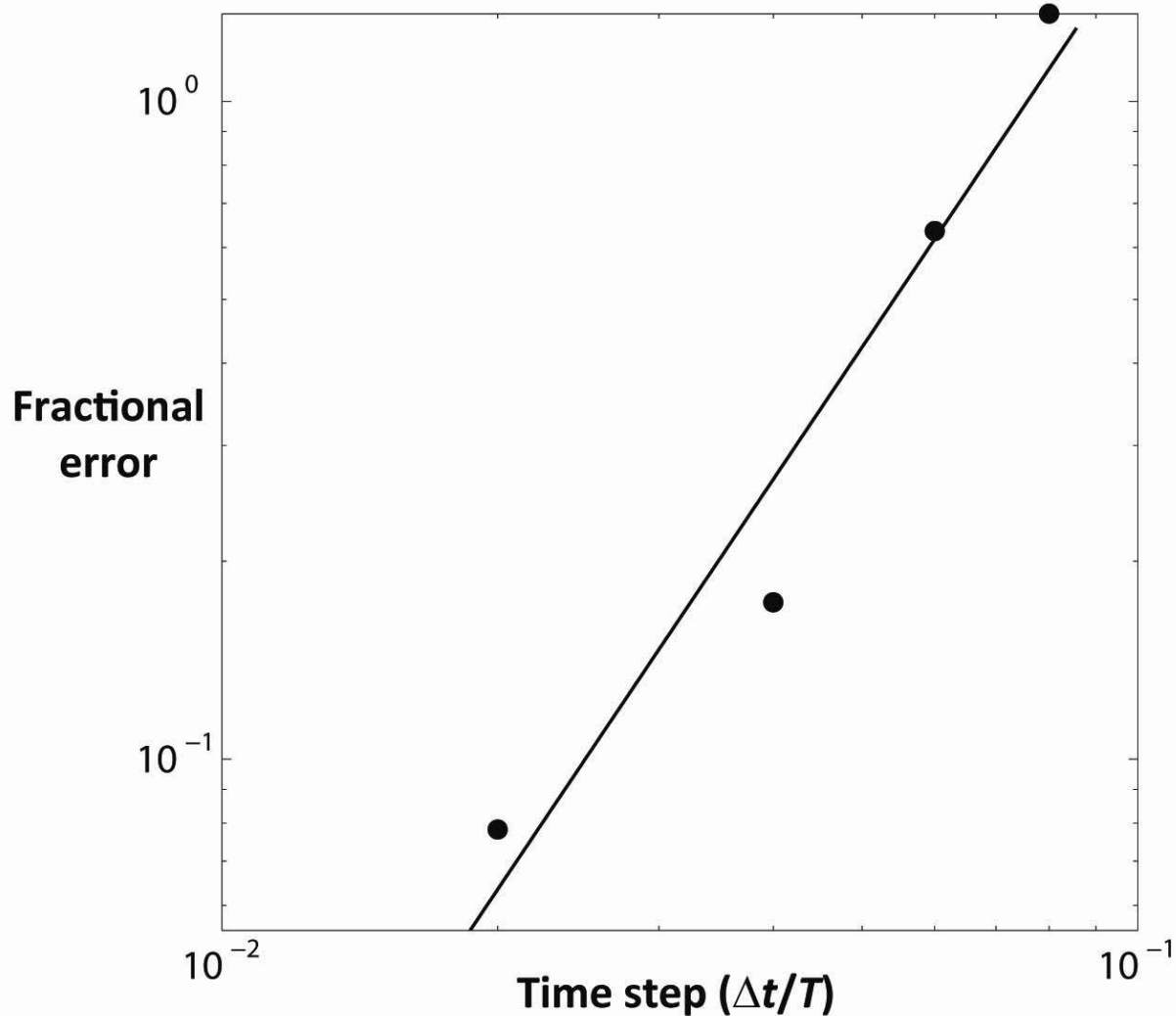
704

705 **Figure A9.** Temporal convergence of the algorithm. Log-log plot of the fractional error in

706 pressure at the head of the simulated three-dimensional self-propelled swimmer versus time step

707 between velocity fields (closed circles). Solid line indicates a slope of 2 corresponding to

708 second-order convergence.

709

710

711 **Figure A10.** Computational cost of the algorithm, as quantified by the time required for a single

712 3-GHz processor to apply the temporal filter (open circles) and to compute the pressure field

713 (closed circles) for velocity fields from 32x32 to 256x256 nodes. Solid line indicates slope of 1.